Ultraviolet laser spectroscopy of neutral mercury in a one-dimensional optical lattice

S. Mejri, J. J. McFerran, L. Yi, Y. Le Coq, and S. Bize*

LNE-SYRTE, Observatoire de Paris, CNRS, UPMC, 61 Avenue de l'Observatoire, FR-75014 Paris, France

(Received 28 June 2011; published 14 September 2011)

We present details on the ultraviolet lattice spectroscopy of the $(6s^2)\ ^1S_0 \leftrightarrow (6s6p)\ ^3P_0$ transition in neutral mercury, specifically ^{199}Hg. Mercury atoms are loaded into a one-dimensional vertically aligned optical lattice from a magneto-optical trap with an rms temperature of $\sim$60 μK. We describe aspects of the magneto-optical trapping, the lattice cavity design, and the techniques employed to trap and detect mercury in an optical lattice. The clock-line frequency dependence on lattice depth is measured at a range of lattice wavelengths. We confirm the magic wavelength to be 362.51(0.16) nm. Further observations to those reported by Yi *et al.* [Phys. Rev. Lett. **106**, 073005 (2011)] are presented regarding the laser excitation of a Wannier-Stark ladder of states.

DOI: 10.1103/PhysRevA.84.032507 PACS number(s): 32.30.Jc, 37.10.Jk, 32.10.Dk, 42.62.Fi

I. INTRODUCTION

The development of an optical clock based on the doubly forbidden $^1S_0 \leftrightarrow {}^3P_0$ transition in neutral mercury incorporates several areas of study including lattice trapping, deep ultraviolet spectroscopy, and notably, frequency metrology. Optical lattices are employed in an array of disciplines in the field of many-body physics [1]; for example, the analysis of quantum phase transitions [2], atom interferometry with Fermi gases [3], the measurement of forces at the micrometer scale [4–6], counting ultracold atoms [7], quantum gravimetry [8], and quantum information systems [9]. Optical clocks have become another means of testing the properties of these optical lattices [10–13].

Narrow line spectroscopy in the deep-ultraviolet (UV) region has been steadily growing since the groundbreaking experiments on the $1S$-$2S$ transition in hydrogen (two-photon: 243.1 nm) [14–16] and the electric-quadrupole transition of $^{199}Hg^+$ (281.6 nm) [17,18], the latter developed as an optical frequency standard. Two further ion clocks have been constructed with transitions in the deep-UV region; those of $^{115}In^+$ (236.5 nm) [19,20] and the sympathetically cooled $^{27}Al^+$ (267.4 nm) relying on the quantum logic spectroscopy of $^9Be^+$ [21,22] or $^{25}Mg^+$ [23].

Laser spectroscopy of neutral cold atoms in the deep-ultraviolet region is a burgeoning field. Recent work includes (i) generating 253.7 nm light for four-wave mixing in mercury to produce continuous Lyman-α radiation for the awaited laser cooling of antihydrogen [24] and (ii) magneto-optic trapping of Hg for an anticipated ultraprecise frequency standard [25,26]. Further work is directed toward producing cold Hg_2 molecules by photoassociation [27]. In addition, a new laser source has been developed that is expected to improve the reliability of laser cooling of mercury [28].

Our main motivation for lattice trapping mercury is to develop a high-performance frequency standard. Mercury is the third element to be investigated for use as an atomic lattice clock [the ^{24}Mg $(3s^2)\ ^1S_0 \leftrightarrow (3s3p)\ ^3P_1$ transition is also being explored as a potential lattice clock [29,30]]. Recently we reported on lattice trapping and spectroscopy of ^{199}Hg with the determination of the Stark-shift free (magic) wavelength associated with the clock transition [26]. Here we provide additional measurements supporting these results and a more extensive description of the experiment, detailing aspects of the magneto-optical trap (Sec. II), the lattice trap (Sec. III), and the ultraviolet spectroscopy (Sec. IV). We end with results pertaining to the delocalization of Wannier-Stark states across adjacent lattice sites.

The relevant energy levels for neutral mercury are illustrated in Fig. 1. The level structure is shared with other alkaline-earth-metal-type neutral atoms, such as Sr and Yb. As the atomic mass increases, the lifetimes of the $^1P_1$ and $^3P_{1,2,3}$ levels become shorter due to the stronger spin-orbit coupling (and higher line frequency). The $^1S_0 \leftrightarrow {}^1P_1$ transition at 185 nm is particularly broad at a linewidth of $\Gamma/(2\pi) =$ 120 MHz, making laser cooling on this line rather inefficient (the Doppler cooling limit is 2.9 mK). Given also that 185 nm laser light is difficult to generate, only the $^1S_0 \leftrightarrow {}^3P_1$ transition at 253.7 nm is used here for laser cooling with $\Gamma/(2\pi) = 1.3$ MHz and a corresponding Doppler cooling limit of 31 μK.

The clock transition is the doubly forbidden $(6s^2)\ ^1S_0 \leftrightarrow (6s6p)\ ^3P_0$ transition, which is very weakly allowed in fermions due to the hyperfine interaction involving the nonzero spin of the nucleus [31]. The same transition can be magnetically induced in the case of bosonic isotopes [32,33]. The influence of the transition to external fields is described in some detail in [25]. Mercury has several favorable features for use as a frequency standard. Its high vapor pressure at room temperature removes the need for an oven. It contains six isotopes with more than 5 % abundance, two of which are fermions (listed in Fig. 1). The fermions have low nuclear spin, which simplifies the complexity of the magnetic substates, and for the spin-$\frac{1}{2}$ ^{199}Hg isotope the tensor polarizability vanishes. It also has a relatively strong sensitivity to tenable changes in the fine-structure constant ($\frac{\partial \ln F_{Hg}(\alpha)}{\partial \ln \alpha} = 0.81$ [34]), permitting tests of such variations with comparisons against ^{87}Sr, for example. Another advantage in comparison to Sr and Yb is the Hg clock transitions's lower sensitivity to blackbody radiation (by more than an order of magnitude [25,35]), which arises because of its lower atomic (dc) polarizability and higher transition frequency. Frequency uncertainties related to blackbody radiation dominate the uncertainty budgets of Sr

*sebastien.bize@obspm.fr

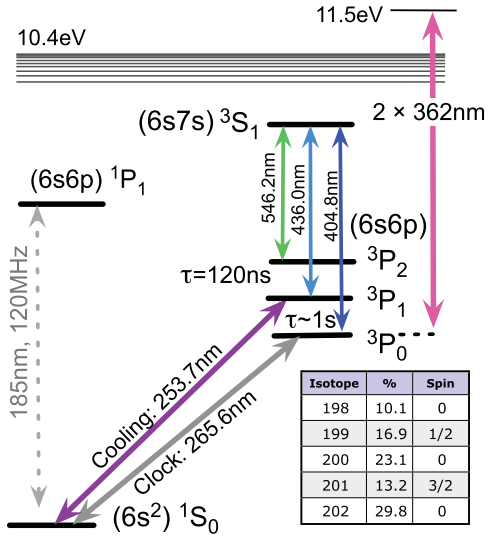

Isotope	%	Spin
198	10.1	0
199	16.9	1/2
200	23.1	0
201	13.2	3/2
202	29.8	0

FIG. 1. (Color online) (a) Relevant energy levels for neutral mercury, not to scale (hyperfine structure for the fermions is omitted). Vacuum wavelengths are shown. Repumping with the $^3S_1$ level is expected to be used in future experiments. Inset: table of isotopic abundance for the isotopes studied here. Not shown: ^{196}Hg (0.15%) and ^{204}Hg (6.9%).

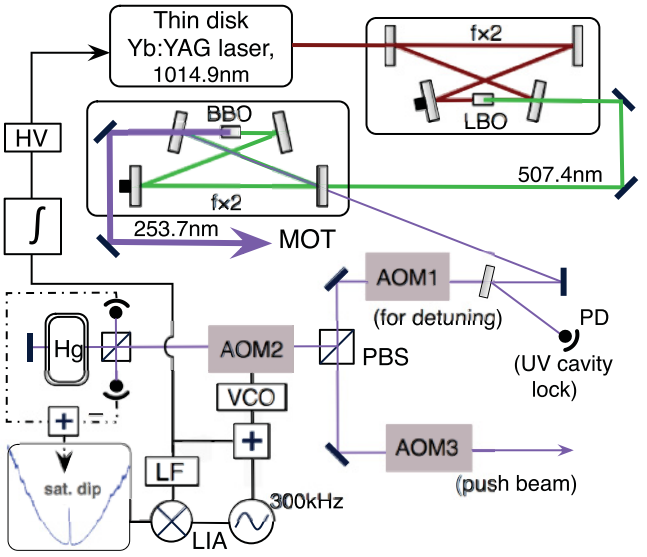

FIG. 2. (Color online) Schematic of the Yb:YAG disk laser frequency control. AOM, acousto-optic modulator; BBO, beta-barium borate crystal; Hg, mercury vapor cell; HV, high-voltage driver; LBO, lithium triborate crystal; LIA, lock-in amplifier; LF, loop filter (including integration); PD, photodiode; PBS, polarizing beam splitter; VCO, voltage-controlled oscillator.

and Yb and will be difficult to reduce to the low 10^{-17} level. On the downside, the lower (ac) polarizability means higher intensities are needed to produce lattice trapping at the same potential well depth.

To enhance the signal-to-noise ratio (S/N) of the clock signal, manipulation of the atoms between the $^3P_{1,2,3}$ levels and $^3S_1$ state can be employed; e.g., for normalized atom number detection and to aid in further cooling of lattice bound atoms. At this stage these repumping wavelengths have not been used. The transition into the continuum, shown in Fig. 1, corresponds to the two-photon ionization induced by the lattice light at 362.5 nm. From [25], the two-photon ionization rate ($\sim 2 \times 10^{-4}$ s^{-1} at 50 kW cm^{-2}) is nearly two orders of magnitude smaller than the off-resonant single photon scattering rate of the lattice lasers.

II. MAGNETO-OPTICAL TRAP

A. Design

The apparatus is composed of two vacuum chambers: one contains the mercury source and has capability for a two-dimensional (2D) magneto-optical trap (MOT), while the other is the main science chamber containing a three-dimensional (3D) MOT and the lattice cavity optics (henceforth, the lattice chamber). A few grams of mercury (with natural isotopic abundance) is contained in a copper crucible within the source chamber and is cooled to approximately -40 °C using a two-stage thermoelectric cooler, which consumes $\sim$1.6 W of electrical power. A 1.5-mm-diam., 10-mm-long conduit creates a pressure differential between the chambers (conductance $= 1.5 \times 10^{-5}$ m^3 s^{-1} for Hg) and simultaneously forms an effusing atom beam in the direction of the MOT.

The MOT is produced by the intersection of three orthogonal pairs of retroreflected σ^+-σ^- polarized UV laser beams with a diameter of $\sim$15 mm. Only one arm of the MOT's laser beam array lies in the horizontal plane. Anti-Helmholtz coils generate the magnetic quadrupole field with a gradient of 0.10 T m^{-1} (10 G cm^{-1}) along the axis of the coil pair at the MOT center. The 253.7 nm light frequency stabilization is carried out with saturated absorption in a 1-mm-long quartz cell containing Hg vapor at $\sim$0.25 Pa at room temperature. The stabilization scheme is shown in Fig. 2. A residual reflection of UV light from the 507.4 nm resonant doubling system is used for frequency stabilization and tuning purposes. This auxiliary beam is frequency shifted by two acousto-optic modulators (AOM-1 and AOM-2) with opposing first-order Bragg diffraction. This allows frequency tuning of the main UV beam with respect to the mercury cell resonance. Sufficient signal is obtained with $\sim$500 μW ($\phi \sim 0.5$ mm) of UV light at the Hg cell for most isotopes. Negative feedback creates a fast servo loop with AOM-2, the correction signal of which is integrated and sent to a piezotransducer in the Yb:disk laser controlling the laser cavity length. The servo bandwidth to the Yb:disk laser is $\sim$3 kHz and produces a laser linewidth of $\sim$100 kHz in the UV. AOM-1 of Fig. 2 is used to detune the frequency of the main MOT beam ($\delta = f_{\text{AOM-2}} - f_{\text{AOM-1}}$), while an additional beam through AOM-3 is used to monitor the Hg partial pressure in the vacuum chamber as well as aid in alignment of the lattice light (through MOT tracing). It may also be used as a second means of estimating the number of atoms in the MOT. The nominal power levels for the wavelengths shown in Fig. 2 are 4 W of 1014.9 nm, 2 W of 507.4 nm, and 40–80 mW of 253.7 nm light.

We capture the fluorescence exiting the lattice chamber through a window concurrent with the horizontal arm of the MOT scheme. The arrangement shown in Fig. 3 is used to simultaneously operate the MOT and record the signal

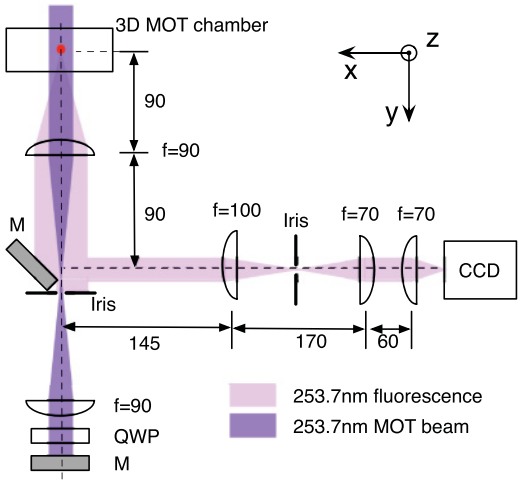

FIG. 3. (Color online) Experimental setup used for imaging of the magneto-optical trap (MOT) and lattice-trapped atoms. The viewing port coincides with one of the arms of the MOT. All dimensions are in millimeters. The z direction is vertical and the x and y directions equate with those shown in Fig. 9. QWP, quarter wave plate; M, mirror; f, focal length.

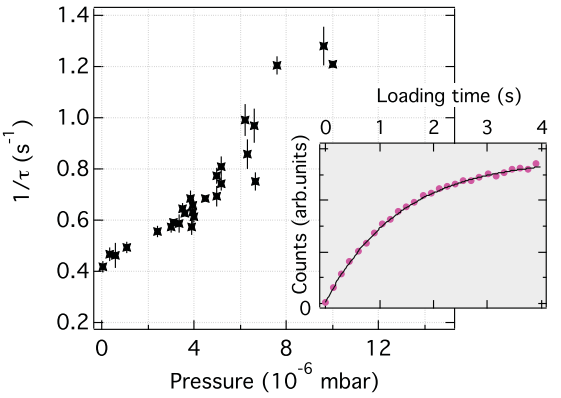

FIG. 4. (Color online) Inverse loading time of the MOT versus the pressure of the Hg source chamber. Inset: an example of a MOT loading curve for ^{200}Hg.

fluorescence. A magnification of 1.1 is used. Approximately 0.2% of the fluorescence reaches a cooled, electron multiplied charge-coupled device (CCD) camera. The number of atoms in the MOT or lattice is determined using $N_a = \Sigma e/(\eta G f \gamma_p \Delta t)$, where Σ is the number of relevant CCD counts, $e = 22.4$ is the CCD sensitivity in terms of electrons per registered count, η is the quantum efficiency of 0.33 ± 0.05 (for a back-illuminated CCD at 254 nm), G is the electron multiplication gain, f is the collected fraction, γ_p is the scattering rate, and Δt is the CCD exposure time. The scattering rate follows from $\gamma_p = s_0\Gamma/[1 + s_0 + (2\delta/\Gamma)^2]/2$, where s_0 is the UV intensity (six beams) normalized by the saturation intensity, $I_s = 102$ W m^{-2}. We ignore interference effects between the beams and any complex behavior of the atoms in the MOT (atom number estimates based on the absorption of a resonant beam agree within a factor of 2 [36]). Our detection is carried out at a detuning frequency of $\delta \sim -\Gamma$, therefore, the factors affecting the counts-to-atoms ratio are the intensity of the 253.7 nm light, the exposure time, and electron multiplication (EM) gain; for example, $s_0 = 4$, $\Delta t = 10$ ms, and $G = 20$ gives $\sim$10 counts per atom.

To release atoms from the MOT, the UV and magnetic fields are switched off, then to detect (with reduced stray light) only two UV beams are switched back on; the horizontal beam remaining blocked (this also minimizes the likelihood of recapturing atoms in a MOT). The sequencing operation of electromagnetic shutters, magnetic field, UV detuning and CCD camera is computer controlled with a multichannel data acquisition board (NI USB-6229).

The conduit between chambers provides high differential pumping with a pressure ratio of typically 10^{-3}. The source chamber pressure is measured by comparing the absorption of a low intensity ($\sim$5 W m^{-2}) 253.7 nm probe beam through the 24-cm-long chamber when the UV light is on and off resonance. The partial pressure of isotope A is found using $p_A = -k_B T \ln(I/I_0)/(\sigma l)$, where σ is the light absorption cross section with $\sigma/(k_B T) = 1.39\times10^4$ Pa^{-1} m^{-1}, l is the length of the source chamber, and I and I_0 are the transmitted light intensity on and off resonance, respectively. The lifetime of the atoms in the MOT was found to be equivalent to the loading time constant up to at least $N_a \sim 2 \times 10^6$ atoms. This was established by comparing the loading time to the decay time when the 2D MOT light was switched off (at a time when the 2D MOT was in use) [36]. The inset of Fig. 4 shows a typical loading curve for ^{200}Hg with a time constant of 1.4 s.

This loading time can be varied (over hours or days) by a change of the source chamber pressure, as seen in the main plot of Fig. 4. The data follow the expected linear relationship between $1/\tau$ and p up to at least 7×10^{-6} mbar. The experiment is not normally run at the higher pressures shown here: the nonlinearity may be due to an unexplored systematic effect. The uncertainties on the pressure measurements also tend to be larger at higher pressure where instabilities in the light level transmitted through the chamber have been observed (despite active intensity stabilization preceding the chamber). The pressure inside the lattice chamber was also monitored based on the current from the ion pump acting on the chamber. The dependence is approximately linear until a pressure below 4×10^{-9} mbar is reached, where the ion pump current is not considered to be a precise measure of the main chamber pressure at the MOT location. For most of our lattice-trapping measurements the lattice chamber was maintained at $\sim 3 \times 10^{-9}$ mbar and the source chamber at 3×10^{-6} mbar, producing MOT lifetimes of $\sim$1.7 s. Assuming collisions with background Hg atoms from the source chamber are limiting the trap lifetime (justifiable from Fig. 4), we deduce the corresponding cross section from $1/\tau = p\sigma_c\bar{v}/k_B T$ to be $\sigma_c \simeq 5\times10^{-13}$ cm^2, where $\bar{v}$ the mean velocity of the background Hg atoms.

B. Trapping and atom number

By recording the MOT fluorescence versus frequency detuning (δ_{load}) we ascertain the optimum detuning for MOT loading for the various isotopes (for our particular beam parameters). In Fig. 5(a) we show this in terms of atom number for the isotopes: ^{199}Hg, ^{201}Hg, and ^{202}Hg; each of which are magneto-optically trapped separately.

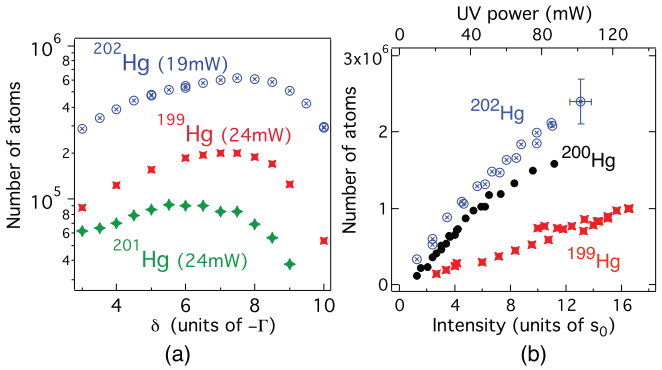

FIG. 5. (Color online) (a) The number of atoms contained in the magneto-optical trap versus frequency detuning for several Hg isotopes. (b) The number of atoms contained in the magneto-optical trap versus UV intensity.

The atom number ratio for the bosons, ^{200}Hg (not shown) and ^{202}Hg, are found to agree with the natural isotopic abundance. However, with regard to the fermions, the level differs from the natural abundance ratio (compare with the values tabulated in the inset of Fig. 1). The ratio for isotopic abundance of ^{199}Hg, ^{200}Hg, ^{201}Hg, ^{202}Hg, and ^{204}Hg can be written as $0.59 : 0.78 : 0.45 : 1 : 0.23$; while for the number of atoms in the MOT, the ratio is found to be $0.32 : 0.80 : 0.12 : 1 : 0.25$ (at $s_0 = 10$). The difference may be attributed to different capture efficiencies between fermions and bosons (or to the modification of the fluorescence rate in the case of the fermions due to their hyperfine structure—for the comparisons here, we assume this not to be the case). Figure 5(b) displays the number of MOT atoms versus intensity for isotopes ^{199}Hg, ^{200}Hg, and ^{202}Hg. There is a clear difference in the number of atoms trapped between the two bosons and ^{199}Hg. At $13I_s$ for the ^{202}Hg (^{199}Hg) isotope we capture 2.4×10^6 (0.83×10^6) atoms in the MOT. The rms cloud radius is 105 μm (110 μm). Based on a Gaussian-shaped cloud with a factor of 2 higher stiffness along the strong axis of the MOT (not seen by the CCD), the corresponding peak densities are 2×10^{11} cm^{-3} and 7×10^{10} cm^{-3}, respectively. One also notices a slight roll-off in the number of atoms for ^{200}Hg and ^{202}Hg at higher intensity, suggesting the onset of saturation effects. The cloud size is observed to increase by less than 10% over the same intensity range, indicating that density limiting factors are not yet prominent.

C. Temperature

In each MOT cycle, after setting the frequency detuning to maximize the number of trapped atoms, a brief period of near-resonance cooling takes place to further lower the temperature. We will henceforth refer to δ as the frequency detuning used during this cooling phase. Temperature and cloud size measurements of magneto-optically trapped mercury were the main focus in article [37]. We will outline some aspects here, since the atom temperature is an important component of trapping atoms in a lattice. With the CCD we are able to record the ballistic expansion of the atom cloud released from the MOT. This is convenient for temperatures in the 30–200 μK range, where expansion is relatively fast. The ballistic expansion is recorded by cycling the MOT and incrementing the release time before each CCD exposure. From the series of images the root-mean-square (rms) radius, $r(t)$ at time t, is deduced and the series of radii is curve fitted by the expression

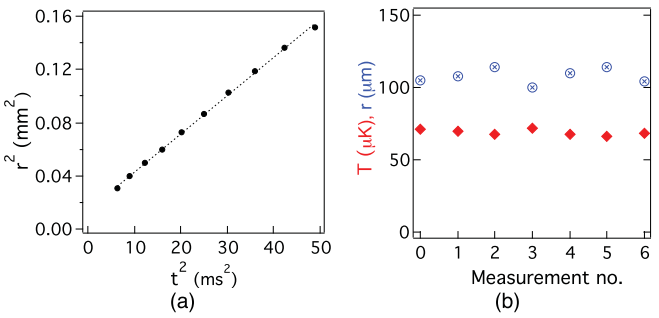

FIG. 6. (Color online) (a) The root-mean-square cloud radius versus release time for the ^{199}Hg isotope at $s_0 = 10.5$. The line fit is based on Eq. (1). (b) A series of cloud size and temperature measurements for the same isotope and intensity. Diamonds, temperature; circles, rms radius.

$$r^2(t) = r_0^2 + (k_B T/M)t^2, \tag{1}$$

where k_B is the Boltzmann constant and M is the atomic mass. This permits an estimation of the temperature, T, and the initial rms cloud size, r_0. An example of the ^{199}Hg cloud expansion is shown in Fig. 6(a) for $s_0 = 10.5$ and $\delta = -\Gamma$ (the line fit produces $T = 68.5$ μK and $r_0 = 119$ μm). Figure 6(b) shows a series of T and r_0 measurements with mean values of 69 μK and 108 μm, respectively, for the same intensity and detuning. This process is used to assess temperature and radius in the discussion below. An example of the MOT profile is shown in the inset of Fig. 7(a) along with a fitted Gaussian line shape.

The duration of the additional cooling phase where δ is brought closer to line center is short compared to the loading phase. This is demonstrated in Fig. 7(a) where we see the cloud temperature as a function of the cooling phase duration. The exponential time constant for ^{199}Hg (^{202}Hg) is 3.7 ms (1.0 ms). The intensity and minimum detuning were different in the two examples with $s_0 = 10.5$ and 3.5, and $\delta = -1.5\Gamma$ and $-\Gamma$ for ^{199}Hg and ^{202}Hg, respectively. Independent of these differences, the change in temperature is seen to be relatively fast and typical of many MOTs with other atomic

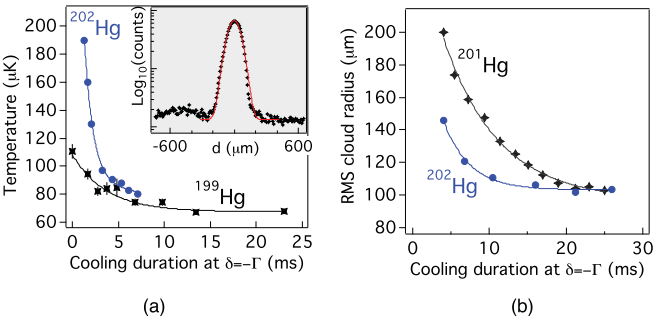

FIG. 7. (Color online) The temperature (a) and root-mean-square cloud radius (b) versus *cooling* duration, where the frequency detuning is reduced to $\delta = -\Gamma$. Inset: intensity profile of the ^{202}Hg MOT with a Gaussian line fit.

elements. During this additional cooling phase the cloud size also decreases as one may expect from [Eq. (3) of [37]]

$$r^2_{i\_\mathrm{rms}} \propto \frac{\Gamma^3}{\delta^2}\frac{1}{s_0}\left(1+s_0+\frac{4\delta^2}{\Gamma^2}\right)^3\frac{\partial B}{\partial x_i}^{-1}, \qquad (2)$$

provided δ is not too close to line center. Here $\partial B/\partial x_i$ is the B-field gradient in the ith direction.

The effect on the cloud size is seen in Fig. 7(b). The exponential time constant is again faster for the bosonic isotope, seen here to be ∼3 ms and 7 ms for ^{202}Hg and ^{201}Hg, respectively. A cooling duration of 20 ms is used in the lattice spectroscopy measurements below. In conjunction with the change in frequency detuning, the magnetic field gradient is doubled for a brief period prior to the atoms' release, which further compresses the atom cloud by ∼15%; the associated time constant is $\lesssim$3 ms.

In [37] we reported agreement between measurement and Doppler cooling theory for the temperature of the bosonic isotopes, and sub-Doppler cooling for the fermionic isotopes. With 30 mW (∼4I_s) of cooling light, a temperature of 70 μK is reached for the bosons, 50 μK for ^{199}Hg, and 35 μK for ^{201}Hg at $\delta = -\Gamma$. Here we present temperature as a function of intensity for the isotopes ^{199}Hg and ^{200}Hg using the ballistic expansion method, but with $\delta = -1.5\Gamma$ (since this produces lower temperatures at the higher intensities). The results are seen in Fig. 8. The upright (inverted) triangle is our previously reported minimum temperature for ^{200}Hg (^{199}Hg). Notable is the difference in slope between the two isotopes at higher intensities. The bosonic and fermionic isotope experiences a slope of 0.062 μK(W m^{-2})$^{-1}$ and 0.016 μK(W m^{-2})$^{-1}$, respectively. This difference in intensity dependence is a further indication that sub-Doppler cooling processes are occurring for the spin-$\frac{1}{2}$ isotope. The solid line [trace (i)] follows from the Doppler cooling theory [38] with $\delta = -1.5\Gamma$ and has a slope of 0.051 μK (W m^{-2})$^{-1}$, similar to that of the ^{200}Hg isotope. The vertical offset may be partly attributed to a bias magnetic field which was in place to displace the MOT into the path of the lattice light (Sec. III), which was observed to increase the temperature by 20 μK (at 10.5s_0). Interestingly, a change in slope is observed at lower intensities, which is less easily explained. Further reduction in temperature occurs at low intensities where $\delta \to -\Gamma$ [as shown by trace (ii) from Doppler cooling theory where $\delta = -\Gamma$]. The hollow circles show the ^{200}Hg MOT temperature for $\delta = -\Gamma$ and falls relatively close to previous measurements. For ^{199}Hg the weak temperature dependence on intensity (and the apparent rise at very low intensities) restricts the minimum temperature to about 50 μK. For comparison, the recoil-limiting temperature is $4\hbar^2k^2/(mk_B) \simeq 6$ μK. The MOT cloud size was recorded simultaneously with the results of Fig. 8. It remained relatively constant for both isotopes at an rms radius of between 100 and 110 μm with a slight increase to 120 μm at the lowest intensities.

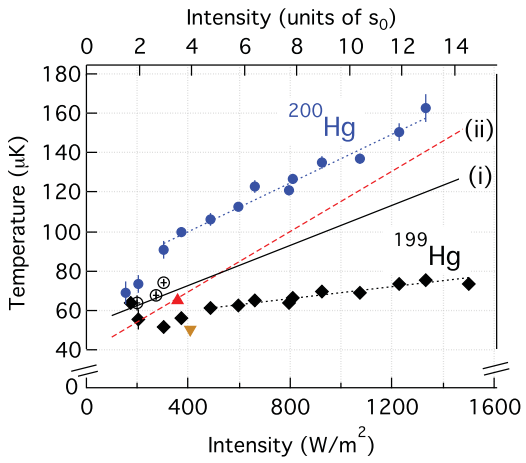

FIG. 8. (Color online) Temperature versus total light intensity at the MOT for ^{200}Hg (filled circles) and ^{199}Hg (diamonds) with $\delta = -1.5\Gamma$. Hollow circles are for ^{200}Hg with $\delta = -\Gamma$. The upright (inverted) triangle is the minimum temperature for ^{200}Hg (^{199}Hg) from [37]. Traces (i) and (ii) are predictions from Doppler cooling theory for $\delta = -1.5\Gamma$ and $\delta = -\Gamma$, respectively.

III. LATTICE TRAPPING

The source for the lattice light is a continuous-wave Ti:sapphire laser. Its broad wavelength tuning provides flexibility for finding the Stark-shift free wavelength. Near 725 nm there is 900 mW of light available for frequency doubling. By use of a Brewster-cut LiB_3O_5 crystal in a bow-tie resonant cavity using the Hänsch-Couillaud locking scheme, ∼200 mW of 363 nm lattice light is produced. A vertically aligned optical cavity, resonant with the 363 nm light, is connected to the main chamber as seen in Fig. 9. The radius of curvature of the mirrors is 250 mm and an indium strip seals the contact between the mirrors and titanium flanges. The flanges are connected to the main chamber via flexible bellows to permit alignment of the mirrors. The 363 nm reflecting optics allow passage for light at 265.6 and 253.7 nm. A 45° planar mirror, set internal to the cavity below the MOT, is designed to remove polarization degeneracy. A phase shift of ∼π per

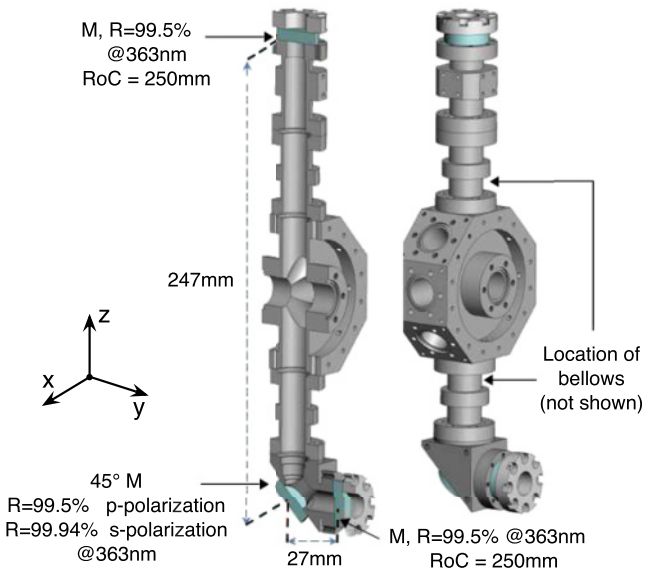

FIG. 9. (Color online) Lattice cavity and 3D MOT chamber. M, mirror; RoC, radius of curvature. The xyz axes provide orientation with respect to Fig. 3. The MOT coils sit in the circular recesses and the ports at 45° allow passage for four of the MOT beams.

round trip occurs between the s and p projections, enabling polarization selection. Here we use the s polarization. This provides a polarizing element suitable for Hänsch-Couillaud locking, where the error signal is returned to a piezo element in the Ti:S laser. A slow integration of the error signal is fed to the piezo actuators on the lattice cavity. The window-free design helps to minimize losses and reduces the level of the scattered light from the intense lattice beam reaching the detection system.

Based on the internal circulating power P of the cavity we can estimate the potential depth of the lattice trap from

$$U_0 = \frac{\alpha_{\mathrm{Hg}}(\lambda_L)}{2c\epsilon_0}\left(\frac{8P}{\pi w_b^2}\right), \tag{3}$$

where $\alpha_{\mathrm{Hg}}(\lambda_L)$ is the ground-state ac atomic polarizability ($\sim 5.3 \times 10^{-40}$ m^3), ϵ_0 is the permittivity of free space, and w_b is the waist size of the lowest-order cavity mode—here equal to 120 μm.

We express the potential depth in terms of the recoil energy, $E_R = \hbar^2 k_L^2/(2m)$, occurring between an atom with mass m and a lattice photon with wave number k_L (and also in terms of the temperature, E_R/k_B). In the parabolic approximation near the bottom of the potential the axial (or longitudinal) trap frequency is

$$f_z = 2\pi\hbar\sqrt{U_0/E_R}/\left(m\lambda_L^2\right), \tag{4}$$

with $k_L = 2\pi/\lambda_L$. Confinement in the perpendicular plane is produced by the transverse Gaussian intensity profile of the trapping beam with a corresponding radial frequency of $f_r = f_z\lambda_L/(\sqrt{2}\pi w_b)$.

Lattice trapping relies on the waist of the lattice cavity being superimposed on the atom cloud in the MOT. Since the rms diameter of the cloud is only $\sim$200 μm, careful displacement of one or the other is required. Here, the easier option is to displace the MOT (in the horizontal plane). Along the coil axis of the MOT, displacement is produced by shunting some current away from one or the other coil. In the perpendicular direction an independent coil is used. The displacement is limited to $\sim$1 mm, beyond which excess distortion and heating of the MOT cloud occurs for efficient lattice loading. To aid in the alignment, a *push* beam (at 253.7 nm), tuned closed to the center of resonance, is prealigned with the MOT center (the alignment is guaranteed by the destruction of the MOT cloud). The lattice light beam is then overlapped with this push beam.

Due to limitations in the level of 363 nm light that could be obtained in the lattice cavity, the well depth is limited to $\sim 15E_R$ ($\equiv$4.5 W, or 5.7 μK) for most measurements. A calculation (Monte Carlo) estimates that 0.1% of the MOT atoms with an rms temperature of 60 μK will be captured into the lattice trap yielding fewer than 10^3 atoms. Given the low atom number and the limited quantum efficiency of Si in the CCD at 253.7 nm, we have implemented a detection scheme to account for stray light fluctuations in the vicinity of the atom cloud (dominated by 253.7 nm detection light). In our CCD background subtraction we consider two regions: (i) a region of interest (ROI) roughly the size of the MOT cloud, and (ii) a circular ring surrounding the ROI with an outer diameter about twice that of the ROI. Prior to the spectroscopy measurements, the ratio of stray light in the ring to that in the

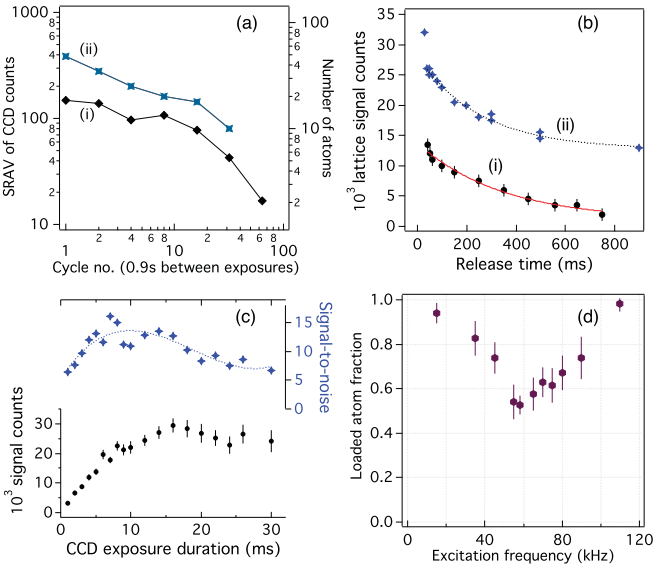

FIG. 10. (Color online) Lattice trapping measurements. (a) The CCD dark noise (i), and the measurement noise floor for atom detection in the lattice (ii) using the square root Allan variance (SRAV) statistic. (b) Lattice lifetime measurements: (i) ^{200}Hg and (ii)^{199}Hg (offset vertically). The release time refers to the duration after the MOT's fields are turned off. (c) Signal (left) and S/N (right) versus exposure duration. (d) Atoms remaining in the lattice versus lattice excitation frequency for ^{199}Hg (MOT release period = 30 ms).

ROI is determined. Then during the spectroscopy this ratio is assumed constant and is used in the cycle-to-cycle processing. We note that the MOT cloud spans approximately 50 pixels in diameter of the CCD (the CCD itself is 512^2 pixels). A demonstration of the detection system sensitivity is shown in Fig. 10(a), where the square root Allan variance (SRAV) of CCD counts versus cycle number is plotted (along with atom number on the right axis). In trace (i) the CCD dark noise was recorded with the camera's physical shutter closed. Trace (ii) shows the measurement noise floor for atom detection, which rises above the dark noise due to the count ratio between the ROI and ring not remaining perfectly constant. This is mainly due to small intensity variations across the profile of the 253.7 nm light beam, which is observed with a small CCD that images light leaking through one of the MOT retroreflecting mirrors.

The timing sequence for the lattice trapping measurements is shown in Fig. 11. Included is the timing of the clock laser probe for the lattice spectroscopy (described in the following section). We define the MOT release period as the interval between when the MOT fields are turned off and the commencement of atom detection (during which time lattice trapping and the clock-line probe occurs). Several tests were carried out to confirm lattice trapping of mercury atoms. Figure 10(b) shows the signal counts versus the MOT release period. The exponential time constant is $\sim$250 ms for ^{199}Hg and $\sim$350 ms for ^{200}Hg. The difference is not expected to be isotopically related but rather due to changes in lattice trapping conditions. These lifetimes are slightly lower than that predicted: a consideration of the intensity noise of the lattice light and parametric excitations [39] suggests that a lifetime of a few seconds should be possible. The disparity could be

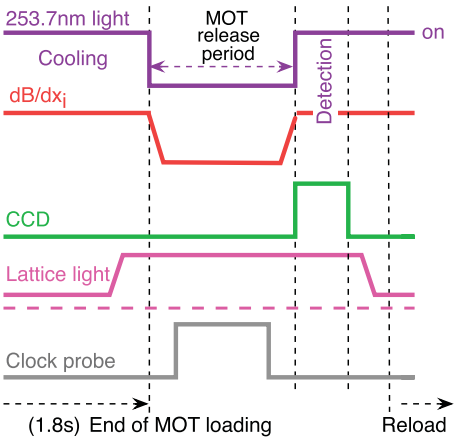

FIG. 11. (Color online) Timing sequence for the lattice trapping measurements and clock transition spectroscopy. For atom detection, only two of the cooling beams are switched back on. For some (earlier) measurements of the $^1S_0 \leftrightarrow {}^3P_0$ center frequency the B-field gradient remained continually on. The MOT release period is also referred to as the lattice trapping period in the text.

due to the distribution of atoms across excited motional states, and/or an underestimate of background collisions. Since the detection process removes atoms from the lattice trap and ROI (due to spontaneous emission in the transverse directions), one expects there to be a given exposure time which optimizes the S/N. This is seen in Fig. 10(c). The lower trace is the difference in counts observed when the lattice light is on and off (the stray lattice light produces about ∼300 counts—a minor fraction). The noise level is determined from the Allan deviation of the counts across the pixels in the ROI under lattice trapping conditions. The MOT release period was 39 ms and the lattice light power ∼4.5 W. The MOT's magnetic field gradient was off during the release period for this measurement. For CCD exposures longer than ∼10 ms the S/N falls, partly due to atom depletion and partly due to an increase in noise (mainly due to the intensity noise across the 253.7 nm beam profile mentioned above). Note, during the release period of 39 ms, the center of mass of the initial MOT cloud has fallen 7.5 mm and expanded to an rms diameter of 3.9 mm. For a uniformly expanding cloud under gravity we estimate that 0.002% of the nonlattice bound atoms remain in the ROI after this time.

Further confirmation of trapping was established by *shaking* the atoms out of the lattice using parametric excitation [39]. A sinusoidal amplitude modulation to the lattice light is applied during the lattice phase in order to excite the longitudinal resonance. Figure 10(d) shows the fraction of atoms remaining trapped as a function of this frequency. We see that maximum depletion occurs close to 60 kHz. Because of the expected distribution over motional states one cannot directly infer that the axial frequency of the trap is half this value. With sideband cooling one expects this trace to narrow and move to higher frequencies [40]. We estimate that f_z is between 40 and 50 kHz. From Eqs. (3) and (4) we infer that the internal cavity power is ∼3 W. A second estimate of the internal power, based on the small level of light transmitted through the 45° reflector in the optical cavity, gives a similar value for the power. A related discussion appears at the end of Sec. IV A.

Four isotopes have been detected in the lattice trap: ^{199}Hg, ^{200}Hg, ^{201}Hg, and ^{202}Hg. In terms of the number of detected counts the ratio is 0.95 : 0.84 : 0.53 : 1, respectively. When compared to the number of atoms in the MOT mentioned above, we see that the lower temperatures of the fermions help increase the fraction of atoms loaded into the lattice.

IV. LATTICE SPECTROSCOPY

A. Magic wavelength

Necessary for the probing of the $^1S_0 \leftrightarrow {}^3P_0$ transition is an exceptionally narrow linewidth light source at 265.6 nm. Described more fully in previous reports [41,42], this is performed through two resonant cavity frequency doubling stages beginning with 1062.6 nm light from a Yb doped fiber laser whose frequency is stabilized with an ultrastable optical cavity. The high finesse cavity (from Advanced Thin Film Inc.) is mounted inside two cylindrical gold-coated aluminum shields, themselves sitting inside two nested vacuum enclosures. The inner vacuum chamber is actively temperature controlled while the gold-coated shielding provides passive isolation of the remaining temperature fluctuations. The optical cavity is composed of two fused silica mirrors optically contacted to an ultralow expansion (ULE) spacer, 100 mm in length. The cavity stabilized 1062.6 nm laser has demonstrated a fractional frequency stability of 5.6×10^{-16} [41] by comparison with a similarly designed cavity, but horizontal in orientation. Acceleration sensitivities were measured to be 3.5×10^{-12} $(\mathrm{m\ s^{-2}})^{-1}$ for the vertical direction and 1.4×10^{-11} $(\mathrm{m\ s^{-2}})^{-1}$ for orthogonal horizontal directions [41].

The ultrastable laser light is delivered to the main Hg experiment via 10 m of polarization maintaining fiber. About 400 μW of this light is used to injection lock a 250 mW distributed feedback diode (DFB) laser, which acts as the light source for frequency quadrupling. The two frequency doubling stages are described in [42]. Residual light from the DFB laser travels through the same fiber in the reverse direction. It is frequency shifted by an AOM and heterodynes with the 1062.6 nm light by use of a beam splitter and photodiode, as depicted in Fig. 12. The fiber noise on the beat note is suppressed through feedback to the AOM. Not shown in this figure is a similar scheme used to cancel the noise on the fiber link between the ultrastable laser and the frequency comb (but using a partial reflector). To scan the UV frequency the drive frequency of the AOM is swept indirectly by varying the frequency of the synthesizer labeled SG in Fig. 12.

The timing sequence for the UV spectroscopy is similar to that described above with the addition of the clock laser probe at 265.6 nm (Fig. 11). The B-field gradient was left on during the clock-transition probing for some of the measurements to maintain higher numbers of atoms (subsequent tests showed that abrupt switching of the B-field gradient produced a loss of atoms in the lattice trap). One scan of the clock transition, at a given lattice wavelength and depth, consisted of at least four consecutive sweeps and required, on average, 180 s of acquisition time. Figure 13(a) shows an example of the $^1S_0 \leftrightarrow$

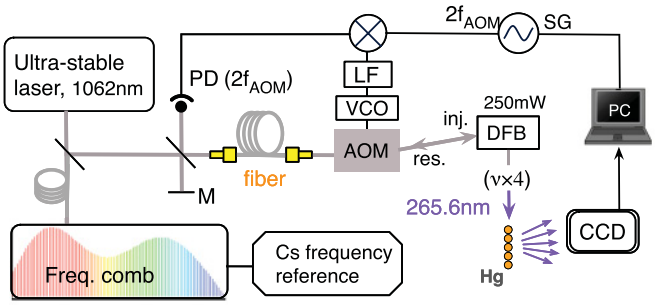

FIG. 12. (Color online) Fiber noise cancellation scheme and UV frequency tuning method. A similar fiber noise cancellation technique is used for the link to the frequency comb, but is not shown here. AOM, acousto-optic modulator; DFB, distributed feedback laser; inj., injection lock; LF, servo loop filter; M, mirror; PD, photodiode; res., residual light from the DFB laser; SG, signal generator; VCO, voltage-controlled oscillator.

$^3P_0$ transition spectrum taken with the $\lambda_L = 362.151$ nm (0.46 nm away from the Stark-shift free wavelength, λ_m).

The line center and width were determined using both Lorentzian and Gaussian line fitting (one may expect to use a sinc^2 line shape, but the difference is not important here due to the low S/N). Where there was a difference in line center (Lorentzian vs Gaussian), we took the mean value or discarded

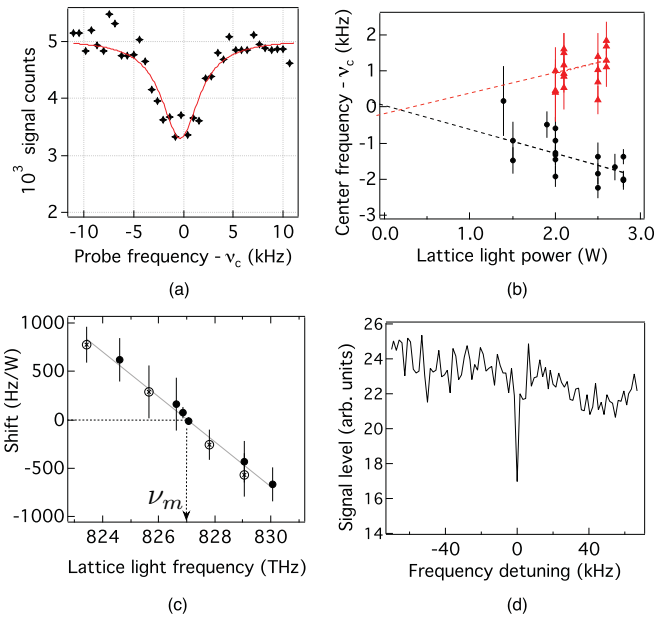

FIG. 13. (Color online) (a) Profile of the ^{199}Hg clock transition at a lattice wavelength of 362.151 nm. The fitted line is a Lorentzian profile. $\nu_c = 1\,128\,575\,290\,808\,400$ Hz. (b) Line-center frequency versus lattice light power at 361.172 nm (830.055 THz) (circles) and 363.556 nm (824.611 THz) (triangles). (c) Differential light shift (Hz W^{-1}) versus lattice light frequency. The lattice frequency where the shift crosses 0 Hz W^{-1} corresponds to the magic wavelength. See text regarding the hollow data points. ν_m, magic frequency. (d) A broader scan of the ^{199}Hg clock transition with the blue sideband apparent.

the measurement. The frequency is offset by the value for the ^{199}Hg line reported in [43], i.e., $\nu_c = 1\,128\,575\,290\,808\,400$ Hz. Frequency measurements and drift rate of the probe light were measured at least three times per day during the course of the measurements. This enabled the frequency of the probe signal to be determined with close to Hz-level uncertainty. Over 130 scans were recorded at various lattice wavelengths and trap depths. Two examples of the line-center frequency dependence on lattice light power are shown in Fig. 13(b), for $\lambda_L = 361.172$ (circles) and 363.556 nm (triangles). An extrapolation of the lines of best fit intersect close to ν_c, providing a measure of self-consistency. Similar measurements were made for ten different lattice wavelengths and the slope of the center frequency dependence on lattice power (or differential light shift) determined for each. These are plotted in Fig. 13(c). The hollowed points correspond to data where 0 Hz was used as the ordinate intercept with an uncertainty of 400 Hz (since there was insufficient variation in lattice power). We consider 400 Hz to be an approximate estimate of the ^{199}Hg clock transition's frequency uncertainty (for the unconstrained data the mean of the intercept values is -250 ± 230 Hz). The center-most data points with the lower uncertainty were taken more recently, where a lattice depth of $20E_R$ ($\equiv 7.5$ μK) was reached and narrower line profiles produced ($\sim$1 kHz). In addition, the B-field gradient was switched off during the lattice trapping period and the 265.6 nm probe. Where the differential shift becomes zero we determine the magic frequency ν_m to be 826.99(0.34) THz, or $\lambda_m = 362.51(0.16)$ nm. The uncertainty is based on the standard deviation of the residuals of the line fit. The differential light shift deduced from the slope of the line fit is -70 ± 20 mHz E_R^{-1} GHz^{-1} or normalized by the transition frequency, $-6 \pm 2 \times 10^{-17} E_R^{-1}$ GHz^{-1} (where most of the uncertainty is associated with that of the power of the lattice light).

A broader, lower resolution scan of the ^{199}Hg clock line is shown in Fig. 13(d). Of significance is the broad blue sideband that appears at a positive frequency detuning, characteristic of Lamb-Dicke confinement of the atoms. The sideband spectrum can be used to infer a value for the trap depth and the circulating power. The frequency f_z given by Eq. (4), which is derived for a lattice trap approximated with a parabolic potential, gives an upper bound for the vibrational frequencies in the trap. The sideband frequency will be f_z in the limit of a very deep trap with only the lowest level occupied. Here, for a shallow trap with all vibrational states populated, many sideband frequencies below f_z are present. Therefore f_z must be equated with the frequency of the uppermost edge of the blue sideband observed here: approximately 70 kHz, which has corresponding power of 6 W. Based on the light level transmitted through the lattice cavity we estimate the internal power to be 6.1 W, supporting the previous argument. There is a slight indication of a red sideband in this figure, but not sufficient to estimate the temperature. At 6.1 W the calculated trap depth is 7.9 μK.

B. Wannier-Stark delocalization

An important objective for a frequency standard is to produce a resonance with a high quality factor; a Q higher than 10^{14} is now reached in some optical atomic frequency

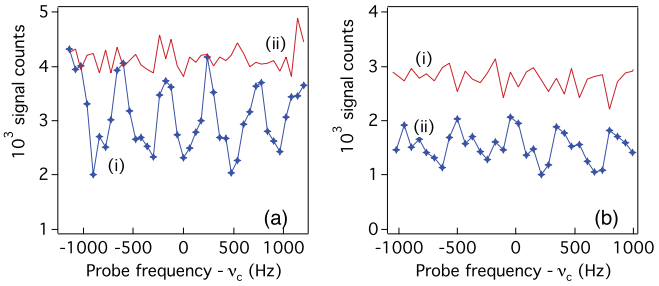

FIG. 14. (Color online) (a) Periodic oscillations brought on by the presence of the 265.6 nm probe light with the B-field gradient off and $U_0 \simeq 8E_R$: (i) probe present for a duration of 20 ms during the lattice trapping period and (ii) probe absent. (b) Demonstrating the effect of the MOT's B-field gradient: (i) B-field gradient on and (ii) B gradient off.

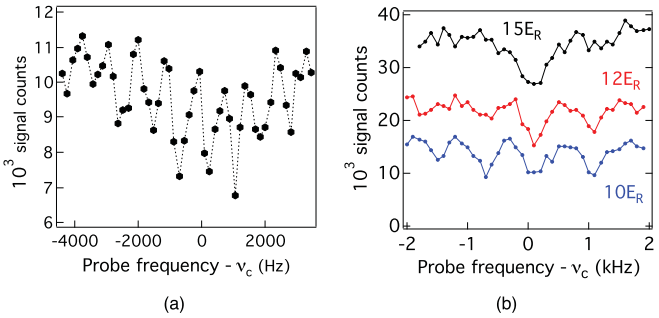

FIG. 15. (Color online) (a) Four higher-resolution scans of the clock transition were recorded every 15 minutes (with the lattice wavelength near λ_m): this plot shows the sum of the four traces with the periodic behavior still evident. (b) Suppression of the Wannier-Stark delocalization by increasing the lattice depth (λ_L = 362.403 nm).

standards [12,17,44–46]. With the goal of producing a narrower line the lattice light was set near the Stark-shift free wavelength, and to minimize line splitting due to the first-order Zeeman effect, the MOT B field was switched off during the lattice and detection periods. Rather than a narrow line, we found a periodic pattern extending across a few kHz when lattice depths were sufficiently low, an example of which is trace (i) of Fig. 14(a), recorded for a trap depth of about $8E_R$ (and λ_L= 362.678 nm). Here, we see the periodic behavior becomes evident with the presence of the 265.6 nm probe light [trace (i)], and is absent without the clock probe [trace (ii)]. The B-field gradient of the MOT also affects the periodic pattern, as seen in Fig. 14(b). With the presence of the MOT B-field gradient the oscillations are imperceivable. A plausible reason for this is that the presence of the MOT field causes a small Zeeman splitting for the lattice trapped atoms that increases with distance from the MOT center (where $B = 0$), and therefore *smooths* out the oscillations. For example, at 100 lattice sites away from the $B = 0$ position of the MOT, the expected shift in the clock transition is ∼20 Hz (for $m_F = -1/2$ to $m_F = 1/2$), while at furthest edges of the lattice of atoms, the shift is ∼120 Hz. The change in Zeeman splitting per lattice site is 0.2 Hz, hence at our resolution of 60–80 Hz the stepped nature of the Zeeman splitting from one site to the next is far from being observable.

As yet there is no deliberate additional cooling of the atoms in the lattice trap, hence there will be some distribution across axial and transverse motional states resulting from the truncated Boltzmann distribution that occurs with lattice trapping of MOT atoms. Wannier-Stark states delocalized over several neighboring lattice sites may then become populated. Therefore, probing of the clock transition can cause excitation along the Wannier-Stark ladder (corresponding to atoms *tunneling* to neighboring lattice sites). There are several results supporting this. First, the 880 ± 10 Hz period of the oscillation matches that of the Bloch frequency, $mg\lambda_L/(2h)$ = 886 Hz, produced by the gravitational potential between lattice sites (within the uncertainty of the measurement). Secondly, the *phase* of the periodic pattern drifts by an indiscernible amount over extended periods of time; for example, Fig. 15(a) shows the averaged sum of four traces recorded over a period of 1 h, with the oscillatory behavior still present. Perhaps the most convincing is that we can suppress the periodic structure by increasing the lattice depth as seen in Fig. 15(b). With a small increase in lattice depth (from $10E_R$ to $15E_R$) the features neighboring the central clock transition become heavily suppressed (this single narrower clock line will be used in future studies of the $^1S_0 \leftrightarrow {}^3P_0$ transition). The controlled tunneling in a vertical optical lattice was recently demonstrated using counterpropagating Raman pulses and showed that the degree of tunneling between lattice sites was enhanced as the lattice depth decreased [47]. We see a similar effect here, but where the tunneling is made manifest by single-photon excitation.

V. CONCLUSIONS

Aspects in relation to magneto-optical trapping and lattice trapping of neutral mercury have been presented; in particular, atom numbers and temperature. We have succeeded in trapping several isotopes of neutral mercury, separately, in a vertically orientated one-dimensional optical lattice. Narrow-line laser spectroscopy at 265.6 nm has been performed on lattice bound ^{199}Hg, demonstrating the light shift dependence of the clock transition on the lattice light wavelength and trap depth. The slope of the differential light shift is -70 ± 20 mHz E_R^{-1} GHz^{-1} (or $-6 \pm 2\times10^{-17} E_R^{-1}$ GHz^{-1}) and the magic wavelength is found to be 362.51(0.16) nm, in support of our earlier measurements [26]. Given this degree of light shift, we expect that the lattice laser frequency will need only be controlled to the levels of a few MHz to reduce first-order light shifts to the low 10^{-18} level. A periodic structure can be made present on the clock transition in well depths less than $\sim 10E_R$, which we attribute to the excitation across a Wannier-Stark ladder of states. This may arise because the atoms are loosely bound in the lattice sites, since the atoms are not forced into the lowest vibrational state. With a deeper lattice trap we can mitigate the delocalizing effects and produce a narrower clock line.

ACKNOWLEDGMENTS

The authors are grateful for the support from the Systèmes de Référence Temps-Espace (SYRTE) technical services. We express thanks to A. Clairon, M. Lours, A. Gérard, S. Dawkins,

and J. Lodewyck for their assistance. J.M. is grateful for the financial support from the Ville de Paris. SYRTE is Unité Mixte de Recherche 8630 of the Centre National de la Recherche Scientifique (CNRS) and is associated with the Université Pierre et Marie Curie (UPMC). This work is partly funded by the Institut Francilien de Recherche sur les Atomes Froids (IFRAF) and by the Centre National d' Études Spatiales (CNES).

[1] I. Bloch, J. Dalibard, and W. Zwerger, Rev. Mod. Phys. **80**, 885 (2008).
[2] M. Greiner, O. Mandel, T. Esslinger, T. Hansch, and I. Bloch, Nature (London) **415**, 39 (2002).
[3] G. Roati, E. deMirandes, F. Ferlaino, H. Ott, G. Modugno, and M. Inguscio, Phys. Rev. Lett. **92**, 230402 (2004).
[4] I. Carusotto, L. Pitaevskii, S. Stringari, G. Modugno, and M. Inguscio, Phys. Rev. Lett. **95**, 093202 (2005).
[5] G. Ferrari, N. Poli, F. Sorrentino, and G. M. Tino, Phys. Rev. Lett. **97**, 060402 (2006).
[6] P. Wolf, P. Lemonde, A. Lambrecht, S. Bize, A. Landragin, A. Clairon, Phys. Rev. A **75**, 063608 (2007).
[7] P. Cheinet, S. Trotzky, M. Feld, U. Schnorrberger, M. Moreno-Cardoner, S. Folling, and I. Bloch, Phys. Rev. Lett. **101**, 090404 (2008).
[8] N. Poli, F. Y. Wang, M. G. Tarallo, A. Alberti, M. Prevedelli, and G. M. Tino, Phys. Rev. Lett. **106**, 038501 (2011).
[9] I. Bloch, Nature (London) **453**, 1016 (2008).
[10] M. Takamoto, F.-L. Hong, R. Higashi, and H. Katori, Nature (London) **435**, 321 (2005).
[11] A. Ludlow *et al.*, Science **319**, 1805 (2008).
[12] N. D. Lemke *et al.*, Phys. Rev. Lett. **103**, 063001 (2009).
[13] P. G. Westergaard, J. Lodewyck, L. Lorini, A. Lecallier, E. A. Burt, M. Zawada, J. Millo, and P. Lemonde, Phys. Rev. Lett. **106**, 210801 (2011).
[14] C. Foot *et al.*, J. Phys. B **23**, 203 (1990).
[15] C. Zimmermann, R. Kallenbach, and T. W. Hansch, Phys. Rev. Lett. **65**, 571 (1990).
[16] M. Niering *et al.*, Phys. Rev. Lett. **84**, 5496 (2000).
[17] R. Rafac, B. C. Young, J. A. Beall, W. M. Itano, D. J. Wineland, and J. C. Bergquist, Phys. Rev. Lett. **85**, 2462 (2000).
[18] W. H. Oskay *et al.*, Phys. Rev. Lett. **97**, 020801 (2006).
[19] J. von Zanthier *et al.*, Opt. Lett. **25**, 1729 (2000).
[20] T. Becker, J. v. Zanthier, A. Y. Nevsky, C. Schwedes, M. N. Skvortsov, H. Walther, and E. Peik, Phys. Rev. A **63**, 051802 (2001).
[21] P. Schmidt *et al.*, Science **309**, 749 (2005).
[22] T. Rosenband *et al.*, Phys. Rev. Lett. **98**, 220801 (2007).
[23] C. W. Chou, D. B. Hume, J. C. J. Koelemeij, D. J. Wineland, and T. Rosenband, Phys. Rev. Lett. **104**, 070802 (2010).
[24] M. Scheid *et al.*, Opt. Lett. **32**, 955 (2007).
[25] H. Hachisu, K. Miyagishi, S. G. Porsev, A. Derevianko, V. D. Ovsiannikov, V. G. Palchikov, M. Takamoto, and H. Katori, Phys. Rev. Lett. **100**, 053001 (2008).
[26] L. Yi, S. Mejri, J. J. McFerran, Y. Le Coq, and S. Bize, Phys. Rev. Lett. **106**, 073005 (2011).
[27] P. Villwock, S. Siol, and Th. Walther, Eur. Phys. J. D (to be published).
[28] J. Paul *et al.*, Opt. Lett. **36**, 61 (2011).
[29] J. Friebe *et al.*, Phys. Rev. A **78**, 033830 (2008).
[30] K. T. Therkildsen, B. B. Jensen, C. P. Ryder, N. Malossi, and J. W. Thomsen, Phys. Rev. A **79**, 034501 (2009).
[31] M. Bigeon, J. Phys. **28**, 51 (1967).
[32] A. V. Taichenachev, V. I. Yudin, C. W. Oates, C. W. Hoyt, Z. W. Barber, and L. Hollberg, Phys. Rev. Lett. **96**, 083001 (2006).
[33] Z. W. Barber, C. W. Hoyt, C. W. Oates, L. Hollberg, A. V. Taichenachev, and V. I. Yudin, Phys. Rev. Lett. **96**, 083002 (2006).
[34] E. J. Angstmann, V. A. Dzuba, and V. V. Flambaum, Phys. Rev. A **70**, 014102 (2004).
[35] S. G. Porsev and A. Derevianko, Phys. Rev. A **74**, 020502 (2006).
[36] M. Petersen, *Laser Cooling of Neutral Mercury and Laser Spectroscopy of the* $^1S_0-^3P_0$ *Optical Clock Transition*, Ph.D. thesis, L'Université Pierre et Marie Curie, L'Observatoire de Paris, 2009 [http://tel.archives-ouvertes.fr/tel-00405200/fr/].
[37] J. J. McFerran, L. Yi, S. Mejri, and S. Bize, Opt. Lett. **35**, 3078 (2010).
[38] P. Lett *et al.*, J. Opt. Soc. Am. B **6**, 2084 (1989).
[39] M. E. Gehm, K. M. O'Hara, T. A. Savard, and J. E. Thomas, Phys. Rev. A **58**, 3914 (1998).
[40] A. Brusch, R. Le Targat, X. Baillard, M. Fouche, and P. Lemonde, Phys. Rev. Lett. **96**, 103003 (2006).
[41] J. Millo, D. V. Magalhaes, C. Mandache, Y. LeCoq, E. M. L. English, P. G. Westergaard, J. Lodewyck, S. Bize, P. Lemonde, G. Santarelli, Phys. Rev. A **79**, 053829 (2009).
[42] S. T. Dawkins *et al.*, Appl. Phys. B: Lasers Opt. **99**, 41 (2009).
[43] M. Petersen, R. Chicireanu, S. T. Dawkins, D. V. Magalhaes, C. Mandache, Y. LeCoq, A. Clairon, and S. Bize, Phys. Rev. Lett. **101**, 183004 (2008).
[44] M. M. Boyd *et al.*, Science **314**, 1430 (2006).
[45] C. W. Chou, D. B. Hume, T. Rosenband, and D. J. Wineland, Science **329**, 1630 (2010).
[46] C. W. Chou, D. B. Hume, M. J. Thorpe, D. J. Wineland, and T. Rosenband, Phys. Rev. Lett. **106**, 160801 (2011).
[47] Q. Beaufils, G. Tackmann, X. Wang, B. Pelle, S. Pelisson, P. Wolf, and F. P. dos Santos , Phys. Rev. Lett. **106**, 213002 (2011).